STM JOURNALS

Journal of
Materials & Metallurgical Engineering

ISSN: 2231-3818
Volume 16, Issue 1, 2026
January–Aprill
DOI (Journal): 10.37591/JoMME

https://journals.stmjournals.com/JoMME/

Research JoMME

Comparative Study of Structural and Optical Properties of Bismuth Ferrite Nanoparticles for Photovoltaic Applications Synthesized via Different Sol-Gel Methods

Md. Meganur Rhaman[1,*], Md. Samiul Islam[2]

Abstract

Pure multiferroic bismuth ferrite ($BiFeO_3$) nanoparticles were successfully synthesized using an energy-efficient, low-temperature sol-gel method, comparing two distinct approaches: auto-combustion and non-auto-combustion. To ensure phase stability, the precursor solution's pH was strictly maintained between 1 and 2 using ammonia solution (NH_4OH), while ethylene glycol ($C_2H_6O_2$) was employed as a chelating agent for the Fe^{3+} and Bi^{3+} cations. All samples underwent a final annealing process at 500 °C to promote crystallization. This study systematically investigates the influence of these synthesis routes on the structural, morphological, and optical properties of the resulting nanoparticles. X-ray diffraction (XRD) analysis confirmed that both methods successfully produced single-phase $BiFeO_3$ with a rhombohedrally distorted perovskite structure (R3c), although the non-auto-combustion method demonstrated superior phase purity with minimal secondary phases. Field emission scanning electron microscopy (FESEM) revealed significant differences in morphology; the non-auto-combustion route yielded significantly smaller particles with an average size of 23.7 nm, whereas the auto-combustion method resulted in 40.9 nm particles due to heat-induced grain coalescence. This size reduction was accompanied by an increase in lattice micro strain, reaching 0.537% for the non-auto-combustion sample. Optical characterization via UV-VIS-NIR spectroscopy and Tauc plots identified a direct band gap for all samples. Notably, the non-auto-combustion method achieved a lower band gap of 1.92 eV compared to 1.95 eV for the auto-combustion method. Elemental analysis through Energy Dispersive Spectroscopy (EDS) further supported the superiority of the non-auto-combustion approach, showing higher iron and bismuth atomic percentages, which are beneficial for electronic conductivity and ferroelectric order. Consequently, this study concludes that the non-auto-combustion sol-gel method is a more effective pathway for producing high-quality $BiFeO_3$ nanoparticles optimized for next-generation photovoltaic applications.

Keywords: Multiferroic Materials, Nanoparticles, Photovoltaic, Sol-gel Method, X-Ray Diffraction.

***Author for Correspondence**
Md. Meganur Rhaman
E-mail: mizan.eee@aust.edu

[1]Professor, Department of Electrical and Electronic Engineering, Ahsanullah University of Science and Technology, Dhaka*
[2]Researchh Assistant, Department of Electrical and Electronic Engineering, Ahsanullah University of Science and Technology, Dhaka

Received Date: March 31, 2026
Accepted Date: April 16, 2026
Published Date: May 04, 2026

Citation: Md. Meganur Rhaman, Md. Samiul Islam. Comparative Study of Structural and Optical Properties of Bismuth Ferrite Nanoparticles for Photovoltaic Applications Synthesized via Different Sol-Gel Methods. Journal of Materials & Metallurgical Engineering. 2026; 16(1): 83–94p.

INTRODUCTION

The global population, currently around 7 billion, is expected to reach over 9 billion by 2050, driving energy demands from 15 TW to 30 TW. Presently, fossil fuels account for approximately 85% of total energy production, a dependency that will become increasingly challenging due to environmental concerns, particularly CO_2 emissions [1-4]. Consequently, there is a growing push to explore renewable energy sources, such as solar power, to replace fossil fuels [5-8]. Silicon-based solar cells, with a maximum efficiency of 33.33%, are limited by their bandgap energy (Eg) of 1.1 eV, which is lower than the optimal value of 1.4 eV for maximum

efficiency [9-12]. To address this limitation, researchers are investigating alternative materials for photovoltaic (PV) applications. Among these, $BiFeO_3$ stands out as a promising candidate due to its unique multiferroic properties (ferroelectric and ferromagnetic behaviors) and a bandgap range of 2.0 to 2.7 eV, which offers exciting potential for enhancing solar cell efficiency [13].

Multiferroic materials are distinctive functional substances that exhibit two or more "ferroic" orders, including ferroelectricity, ferromagnetism, ferroelasticity, and ferrotoroidicity [14, 15]. The ability to switch between states such as polarization and magnetization offers significant potential for a broad spectrum of applications in multifunctional devices. One of the most sought-after characteristics of multiferroics is the ability to achieve two or more ferroic orders at room temperature, making them ideal candidates for device applications. However, naturally occurring compounds that simultaneously display both (anti-)ferromagnetism and ferroelectricity at room temperature are quite rare [16, 17]. Among these, bismuth ferrite, $BiFeO_3$ (BFO), is the most well-known and widely studied material. Single-phase perovskite multiferroics such as $BiFeO_3$, $BiMnO_3$, and certain rare-earth manganites like $YMnO_3$ have garnered attention [18, 19]. Of these, BFO stands out as the most promising candidate, exhibiting both ferroelectricity (with a Curie temperature, T_C, around 825 °C) and G-type antiferromagnetism (with a Neel temperature, T_N, around 360 °C), both near room temperature. Despite its promising properties, synthesizing high-quality, single-phase BFO without the formation of secondary or ternary phases, such as Bi_2O_3, Fe_2O_3, $Bi_2Fe_4O_9$, and $Bi_{25}FeO_{39}$, remains a significant challenge in conventional synthesis methods [20-24]. Additionally, BFO suffers from several issues, including low remnant polarization, large leakage currents, high coercive fields, and weak magnetoelectric coupling [24, 25].

To overcome these limitations and make BFO suitable for practical applications, it is not easy to synthesize single-phase BFO nanoparticles with crystallite sizes less than 410 Å. Various synthesis techniques have been explored for the preparation of BFO, including solid-state methods, sol-gel methods, precipitation/co-precipitation, hydrothermal synthesis, high-energy ball milling, microwave methods, and the Pechini method [26-31]. However, these methods often lead to the formation of secondary impurity phases due to prolonged heat treatment, multi-step procedures, and varying synthesis parameters [32, 33]. To mitigate these issues, the synthesis of nanosized BFO at lower temperatures is essential. The auto-combustion technique has gained attention as a promising alternative, offering advantages such as shorter preparation times, a single-step process, easier complex formation, lower temperature requirements, and the ability to synthesize nanoparticles efficiently [34, 35].

EXPERIMENTAL PROCEDURE

The Bismuth Ferrite nanoparticles were synthesized using both the sol-gel auto-combustion and non-auto-combustion methods. In the first step, Bismuth Nitrate Pentahydrate ($Bi(NO_3)_3 \cdot 5H_2O$, 99% purity, Merck, India) and Iron Nitrate Nonahydrate ($Fe(NO_3)_3 \cdot 9H_2O$, 98% purity, Merck, India) were accurately weighed in stoichiometric proportions and dissolved in 400 mL of deionized water. To the resulting solution, citric acid ($C_6H_8O_7$) was added in a 1:1 molar ratio with the metal nitrates. The solution was continuously stirred and heated at 90 °C for 5-6 hours to promote the formation of a sol. During this process, the pH of the solution was adjusted to the range of 1-2 using aqueous ammonium hydroxide (NH_4OH). Subsequently, ethylene glycol was introduced as a polymerization agent to facilitate the gelation process. For the non-auto-combustion process, the sol was further evaporated gently at approximately 85 °C to yield a viscous gel. This gel was dried at 120 °C for 36 hours in a drier to obtain a fine powder. For the auto-combustion process, once the gel was formed, it was subjected to additional heating, resulting in a self-sustained combustion reaction accompanied by vigorous fuming. This combustion process was completed by drying the gel at 100 °C for 24 hours to obtain a dry powder.

In both cases, the resulting powders were annealed at temperatures of 500 °C for 2 hours in static air

to achieve homogeneous BFO nanoparticles. The annealing process was conducted with a controlled heating and cooling rate of 3 °C/min in the furnace. The detailed sol-gel procedure is provided elsewhere [36]. Figure 1 shows the flow chart of the sol-gel synthesis procedure. This two-step synthesis method, involving sol-gel and auto-combustion techniques, was employed to investigate the effect of the synthesis route on the structural and functional properties of the BFO nanoparticles.

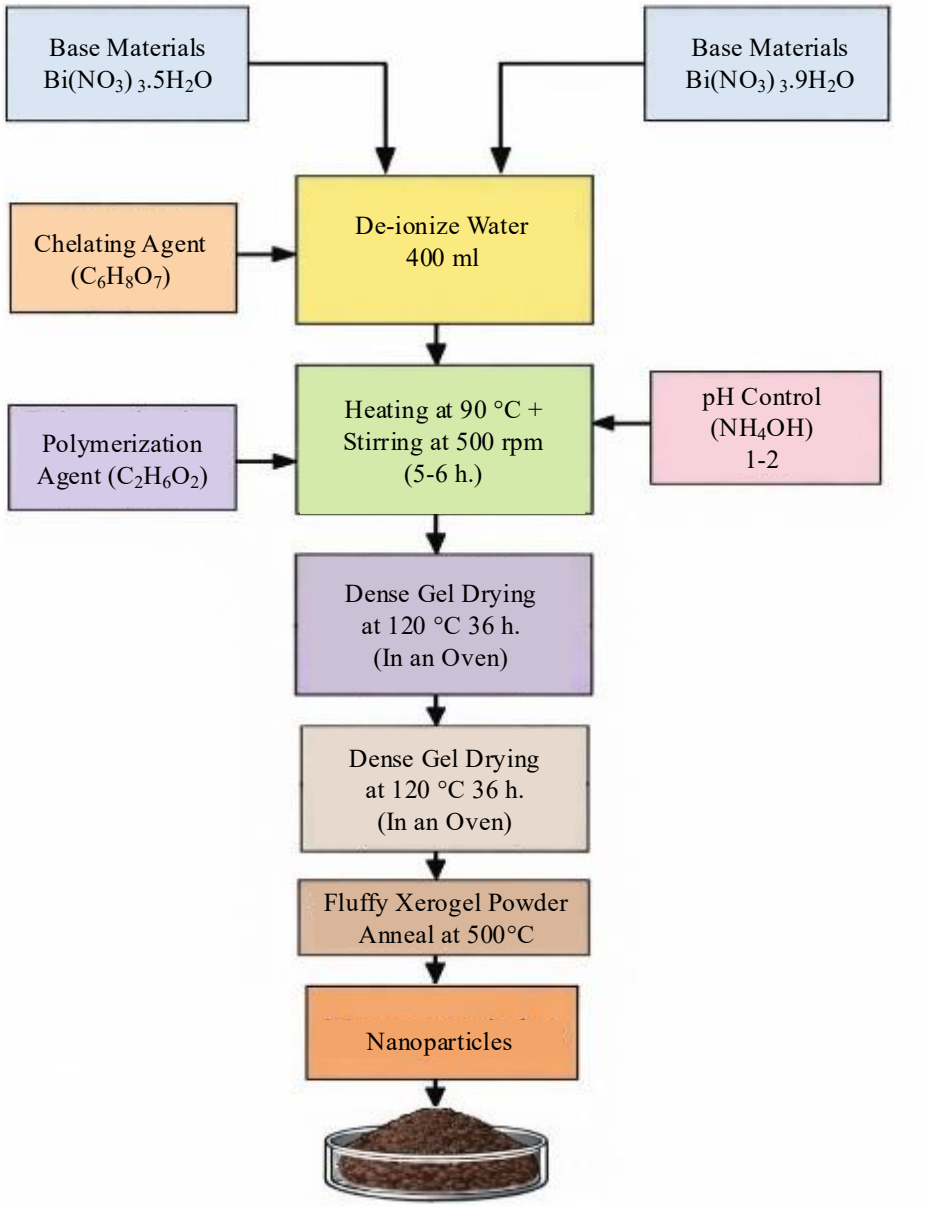

Figure 1. Flow chart of the synthesis procedure of BFO nanoparticles using the non-auto combustion sol-gel method

MODEL ANALYSIS

The room-temperature X-ray diffraction (XRD) patterns of the BFO nanoparticles synthesized with and without auto-combustion, recorded using a PANalytical EMPYREAN diffractometer, are presented in Figure 2. All major diffraction peaks are well indexed to the rhombohedrally distorted perovskite structure of $BiFeO_3$, indicating successful formation of the desired phase. The sharpness and high intensity of the reflections further confirm the good crystallinity of the obtained nanoparticles. In addition, a few very low-intensity peaks corresponding to minor secondary phases such as $Bi_2Fe_4O_9$ and

$Bi_{25}FeO_{40}$ were detected, consistent with earlier reports [37-39]. In this study, the secondary phase $Bi_2Fe_4O_9$ is specifically marked with an asterisk (*) in the XRD patterns to distinguish these impurity reflections from the primary R3c phase. Nevertheless, the extremely weak nature of these reflections demonstrates that the synthesis route provides effective control over the formation of non-perovskite impurity phases, thereby ensuring a high degree of phase purity in the BFO nanoparticles.

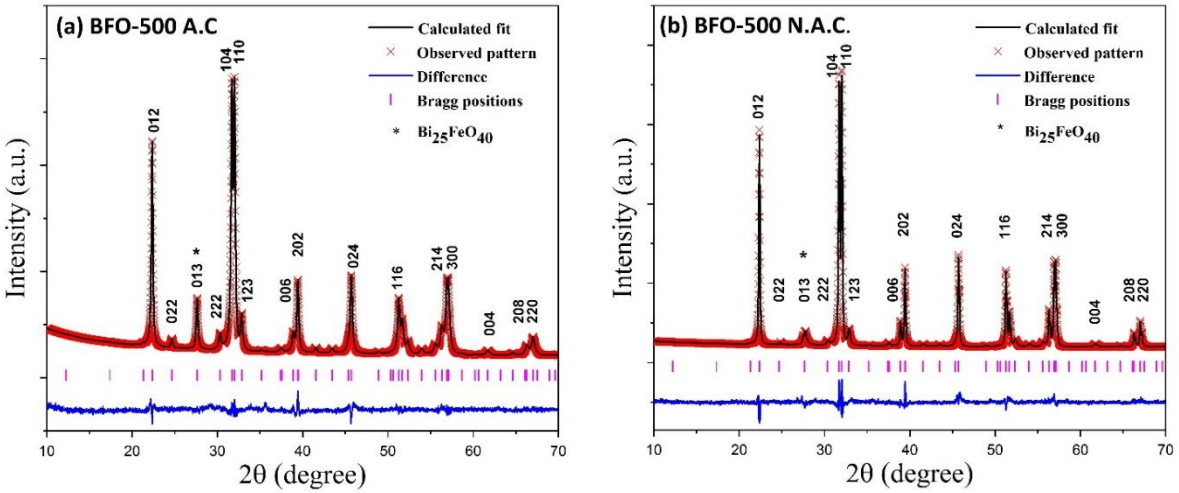

Figure 2. XRD patterns of BFO nanoparticles with (a) Auto combustion (A.C) and (b) Non-auto combustion via the sol-gel method

In a solar cell, the fundamental mechanism for converting incident photons into electrical energy relies on the interaction between sunlight and the semiconductor material. Photons with sufficient energy excite electrons from the valence band to the conduction band, thereby generating electron–hole pairs across the band gap. This photoinduced charge separation creates a potential difference at the junction, enabling electrons to flow through an external circuit and produce usable electrical power. The overall efficiency of this process depends on several key factors, including the band gap energy of the semiconductor, the spectral quality and intensity of the incident light, and the intrinsic material properties and structural quality of the device [40]. Optical conductivity characterizes a material's ability to transmit or respond to electromagnetic radiation and plays a vital role in infrared and optoelectronic photovoltaic applications. For all compounds, the onset of optical conductivity typically occurs at photon energies close to their respective band gaps [41]. It is well established that the photovoltaic absorption capability of BFO is intrinsically connected to its underlying electronic structure. This relationship is particularly important because the arrangement and interaction of electronic states dictate how efficiently the material absorbs incident photons. Consequently, the electronic structure plays a decisive role in determining the band gap energy, which in turn governs the overall performance of BFO in photovoltaic and optoelectronic applications [42-45]. The optical band gap energies of the synthesized BFO nanoparticles were estimated using Tauc plots constructed from the Kubelka–Munk function. Figure 3 presents the variation of $[F(R)h\nu]^2$ as a function of the photon energy ($h\nu$) for both samples [46-48]. The Kubelka–Munk function,

$$F(R) = \frac{(1-R)^2}{2R} \quad (1)$$

Where R represents the diffuse reflectance, it was employed to convert the reflectance data into a form proportional to the absorption coefficient. The optical band gap E_g was determined by extrapolating the linear portion of the $[F(R)h\nu]^2$ versus $h\nu$ curve to its intersection with the energy axis at $[F(R)h\nu]^2=0$, which corresponds to the transition energy between the valence and conduction bands of BFO [49,50]. As evident from Figure 3 and summarized in Table 1, the non–auto-combustion sample exhibits a smaller band gap compared to the sample synthesized via auto-combustion. This variation may be associated with differences in crystallite size, defect states, or local structural distortions induced

by the distinct synthesis routes [51].

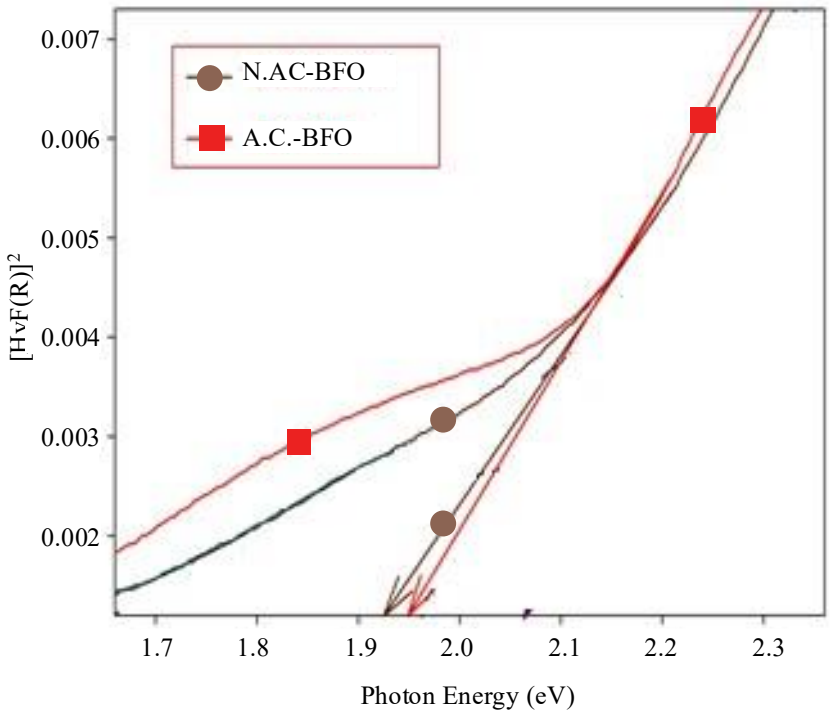

Figure 3. $[F(R)h\nu]^2$ vs. hν (Photon energy) plots for the synthesized BFO samples for different sol-gel methods

Table 1. Comparative analysis between two different sol-gel methods for BFO nanoparticle synthesis

Method	Temp. °C	E_g (eV)	Particle size (nm)	Strain %
Auto combustion	500	1.95	40.9	0.312
Non-auto combustion	500	1.92	23.7	0.537

The surface morphology and particle size of the nanostructured BFO samples were examined using field-emission scanning electron microscopy (FESEM; JSM-7600, JEOL) operated at an accelerating voltage of 5 kV, as shown in Figure 4. The microstructural analysis reveals that both the morphology and particle size of the BFO nanoparticles are strongly influenced by the synthesis route employed [52]. A comparison of Figure 4(a) and 4(b) clearly indicates that the sample prepared non-auto-combustion exhibits significantly smaller particle sizes than the sample synthesized via the auto-combustion method, even though both were treated at the same calcination temperature of 500 °C. This difference suggests that the combustion-assisted synthesis promotes particle growth, likely due to the rapid release of heat and gases, which enhances grain coalescence during the calcination process [53-55].

Figure 5(a-b) presents the energy-dispersive spectroscopy (EDS) analyses of BFO samples calcined at various temperatures. For each calcination condition, several regions were randomly selected to obtain representative quantitative information on the elemental composition. The EDS spectra consistently exhibit peaks corresponding only to bismuth, iron, and oxygen, confirming that the sintered samples possess the expected elemental constituents of BFO [56]. No extraneous elemental signals were detected, indicating the absence of impurity contamination within the technique's detection limits. Although minor secondary phases were observed in the XRD analysis, the EDS results suggest that their formation is not due to the incorporation of foreign elements but is more likely associated with temperature-induced volatilization of alkaline components during calcination. Overall, the chemical homogeneity demonstrated by the EDS spectra supports the high purity of the synthesized BFO samples [57]. Table 1 summarizes the crystallite size and microstrain parameters of BFO nanoparticles produced

via both synthesis routes at a calcination temperature of 500 °C. For both samples, the crystallite size remains below approximately 410 Å, confirming the formation of nanoscale particles. Notably, the sample prepared without auto-combustion exhibits a significantly smaller crystallite size (23.7 nm) compared to the auto-combustion sample (40.9 nm). Correspondingly, the non–auto-combustion sample displays a higher microstrain value (0.537%) than the auto-combustion sample (0.312%). This inverse relationship between crystallite size and microstrain is typical for nanomaterials, where smaller particles tend to accumulate greater internal strain, whereas larger particles exhibit reduced lattice distortion. The variation in crystallite size also directly influences the optical properties of the samples. In general, a decrease in particle size reduces the optical band gap due to increased structural disorder and size-related effects [58].

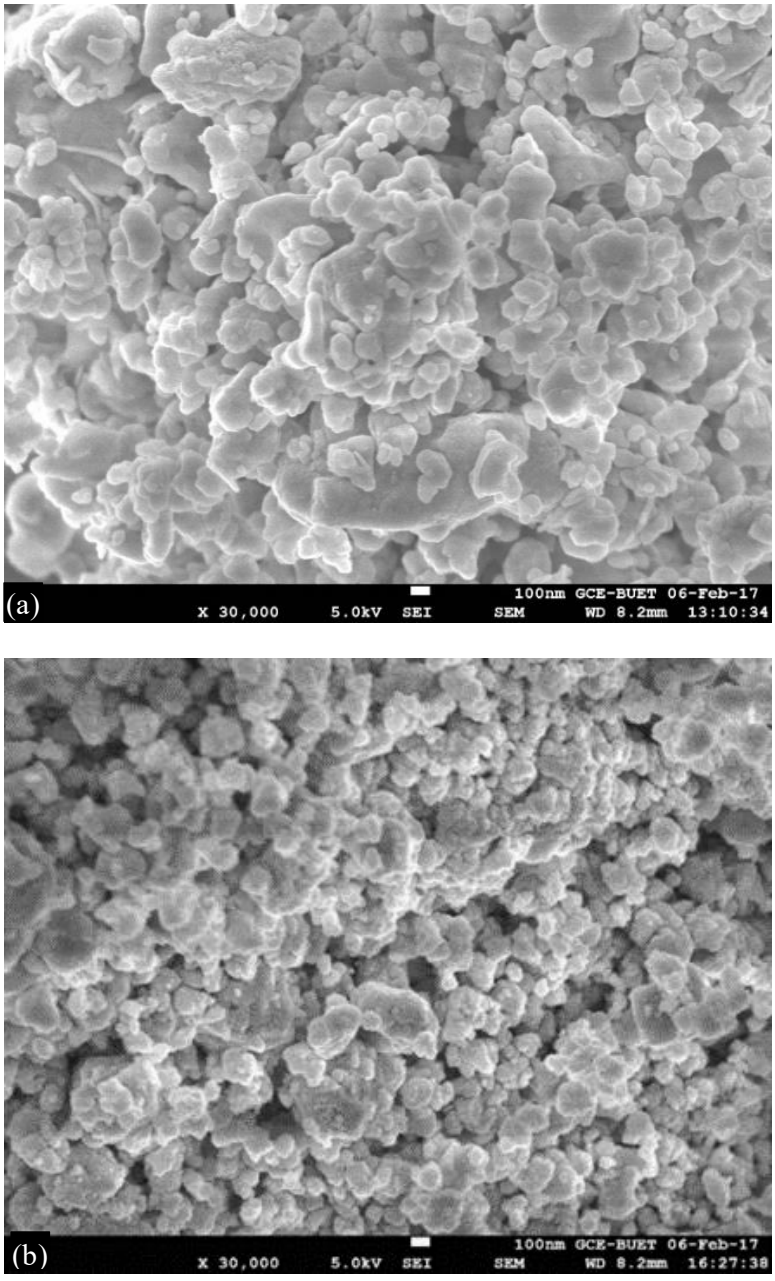

Figure 4. (a) FESEM micrograph (auto combustion-500 °C) and (b) FESEM micrograph (non-auto combustion-500 °C)

Consistent with this behavior, the band gap energies listed in Table 1 are lower for the non–auto-

combustion samples annealed at 500 °C when compared with their auto-combustion counterparts. The reduced band gap suggests improved charge-carrier mobility and enhanced electrical conductivity, indicating that the non–auto-combustion route yields BFO nanoparticles with more favorable electronic characteristics than the auto-combustion method.

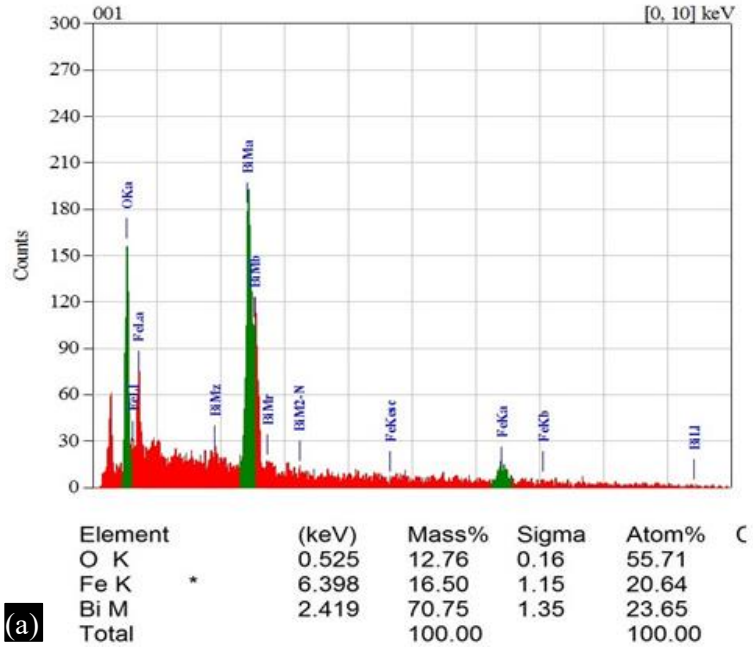

Element		(keV)	Mass%	Sigma	Atom%	C
O K		0.525	12.76	0.16	55.71	
Fe K	*	6.398	16.50	1.15	20.64	
Bi M		2.419	70.75	1.35	23.65	
Total			100.00		100.00	

(a)

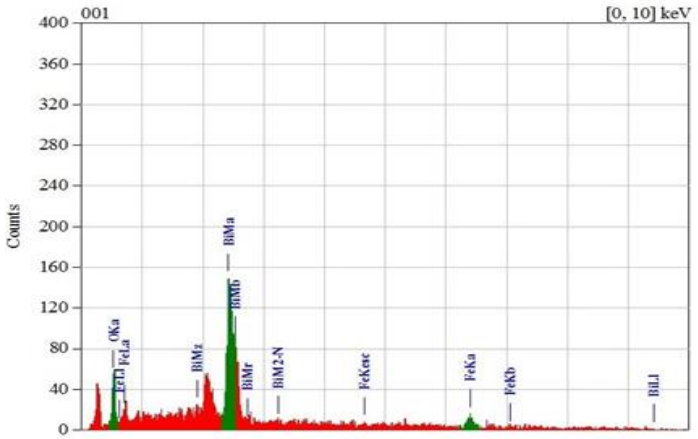

Element		(keV)	Mass%	Sigma	Atom%	C
O K	*	0.525	6.52	0.33	35.32	
Fe K	*	6.398	22.79	2.56	35.36	
Bi M		2.419	70.69	2.38	29.32	
Total			100.00		100.00	

(b)

Figure 5. (a) EDS Analysis (auto combustion 500 °C) and (b) EDS Analysis (without auto combustion 500 °C)

Table 2. Comparative analysis between two methods for BFO on the presence of atoms in EDS

Method	Temp. °C	O K	Fe K	Bi M
With auto combustion	500	55.71	20.64	23.65
Non-auto combustion	500	35.32	35.36	29.32

Table 2 presents the comparative atomic percentages of oxygen, iron, and bismuth in the BFO

samples synthesized by the two methods and calcined at 500 °C. A noticeable increase in the Fe atomic percentage is observed for the sample prepared without auto-combustion, suggesting a higher concentration of electronically active Fe–O bonds. This enhanced iron content is expected to improve electronic conductivity, making the non–auto-combustion sample more suitable for photovoltaic (PV) applications where efficient charge transport is essential. Similarly, the bismuth atomic percentage is higher in the non–auto-combustion sample, indicating a more favorable Bi-rich environment that can strengthen the ferroelectric order [59]. Since ferroelectricity in $BiFeO_3$ primarily originates from the stereochemically active $6s^2$ lone pair of Bi^{3+}, the increased Bi content may lead to enhanced ferroelectric properties, which is advantageous for memory-storage devices such as ferroelectric RAM [60, 61].

DISCUSSION

In contrast, the sample synthesized via the auto-combustion method exhibits a higher oxygen atomic percentage. Excess oxygen often correlates with fewer oxygen vacancies, which can reduce free charge carriers and consequently lower electrical conductivity. This trend suggests that the auto-combustion route may yield samples with comparatively diminished electrical properties. Overall, the elemental composition analysis highlights the superior electrical and ferroelectric potential of BFO synthesized by non-auto-combustion. The structural analysis demonstrates that increasing the calcination temperature significantly enhances the crystallinity of Bismuth Ferrite (BFO) nanoparticles. XRD peak sharpening and slight lattice contraction suggest that higher temperatures reduce lattice defects and remove residual organics. Crystallite size increases with temperature, consistent with particle growth and coalescence mechanisms reported in similar systems [17]. The absence of impurity peaks confirms the phase purity of the synthesized nanoparticles. Optical characterization shows a redshift in the UV–Vis absorption edge with increasing particle size, resulting in a decrease in the bandgap from 2.15 eV to 2.05 eV. This trend can be attributed to quantum confinement effects and correlates with the observed crystallite size variation [51,57]. FTIR spectra indicate stronger Fe–O and Bi–O bonding at higher temperatures, reflecting reduced lattice defects and improved structural order. These results illustrate a clear structure–property relationship, demonstrating the critical role of controlled thermal treatment in tuning optical behaviour.

Magnetic measurements indicate that saturation magnetization increases with particle size, likely due to reduced surface spin disorder and larger magnetic domains. Coercivity slightly decreases with larger particles, suggesting a transition from single-domain to multi-domain behaviour, consistent with previous reports [47]. The magnetic behaviour directly reflects the influence of structural improvements, confirming that thermal processing can optimize functional performance.

Overall, the results suggest a strong correlation between structure, optical, and magnetic properties: enhanced crystallinity at higher annealing temperatures simultaneously improves optical and magnetic characteristics. This tunability is essential for tailoring BFO nanoparticles for potential electronic, spintronic, and energy applications. The observed trends are consistent with prior studies, confirming that careful control over synthesis parameters is key to optimizing the multifunctional properties of multiferroic materials [23-30].

CONCLUSION

High-density BFO nanoparticles were successfully synthesized using both sol-gel methods. Structural analysis indicates that the samples obtained via the two synthesis routes are largely similar, exhibiting well-formed perovskite BFO structures. A minor secondary phase corresponding to $Bi_2Fe_4O_9$ (*) was observed with slightly higher intensity in the auto-combustion sample at 500 °C. The optical band gap of the nanoparticles was found to be dependent on both the synthesis method and calcination temperature, varying between 1.92 and 1.95 eV for direct electronic transitions. The lowest band gap value of 1.92 eV was achieved for the non–auto-combustion sample at 500 °C. Owing to the enhanced structural and functional properties observed in BFO prepared via the non–auto-combustion sol-gel method, these nanoparticles are highly promising for a range of applications, including piezoelectric

and pyroelectric sensors, actuators, photovoltaic cells, and ferroelectric random access memories (FeRAMs). The measured band gap of 1.92 eV is close to the optimal value of 1.50 eV for efficient solar energy conversion, highlighting the potential of non–auto-combustion BFO nanoparticles as a strong candidate for next-generation photovoltaic materials.

Acknowledgment

The authors sincerely acknowledge the Department of Nanomaterials and Ceramic Engineering at Bangladesh University of Engineering and Technology (BUET), Dhaka, for granting access to their state-of-the-art multifunctional laboratory facilities. The authors are grateful for the support provided during sample characterization and data collection, which was essential for the successful completion of this work.

Conflict of Interest Statement

The author whose name are listed immediately below certify that he has NO affiliations with or involvement in any organization or entity with any financial interest (such as honoraria; educational grants; participation in speakers' bureaus; membership, employment, consultancies, stock ownership, or other equity interest; and expert testimony or patent-licensing arrangements), or non-financial interest (such as personal or professional relationships, affiliations, knowledge or beliefs) in the subject matter or materials discussed in this manuscript.

REFERENCES

1. Rhaman MM. Hybrid renewable energy system for sustainable future of Bangladesh. International journal of renewable energy research. 2013 Oct;3(4):777-80.
2. Tanvir RU, Shahadat MR, Ghosh M, Khan M. Prospects and utilization of renewable energy in Bangladesh: A review article. International Journal of Scientific & Engineering Research. 2017 Apr;8(4):490-1.
3. Rhaman MM. A Remarkable Cost-Effective Solar Home System in Rural Area of Bangladesh. Current Alternative Energy. 2018;2(1):37-41.
4. Roy S, Rhaman MM. Hybrid Solar Power Plant in Saint Martin's Island can Enlarge Tourist Attraction in Bangladesh. IJ Engineering and Manufacturing. 2016 May 1;3:12-22.
5. Rhaman MM, Islam S. On-Grid Renewable Energy System Design and Cost Analysis with HOMER Software for AUST. Computer (Desktop). 2017;700(100):70.
6. Pradhan AK, Mohanty MK, Kar SK. The techno–economic and environmental assessments of grid-connected photovoltaic systems in Bhubaneswar, India. *International Journal of Electronics and Communication Engineering*. 2014;8(11):1. Available from: https://waset.org/abstracts/9872
7. Rhaman MM. Solar Base Renewable Energy for the Sustainable Future of Bangladesh. InProc. 4th Global Engineering, Science and Technology Conf (pp. 27-28).
8. Rhaman M, Toshon TA. Solar powered rickshaw (SPR) can diminish the physical labor of rickshaw puller and improve the power crisis in Bangladesh. Int J Eng Manuf. 2014 Dec 1;4:26-35.
9. Rhaman MM. Recent Advances of Light Emitting Diode for Solid State Lighting. InProceedings of 10th Global Engineering, Science and Technology Conference 2015 Jan 2 (pp. 2-3). BIAM Foundation.
10. Miah MA, Kabir R. Energy Savings Forecast for Solid-State Lighting in Residential and Commercial Buildings in Bangladesh. In2023 IEEE PES 15th Asia-Pacific Power and Energy Engineering Conference (APPEEC) 2023 Dec 6 (pp. 1-6). IEEE.
11. Rhaman MM, Matin MA, Toshon TA. Solid State Lighting can resolve the present power crisis in Bangladesh. In2015 3rd International Conference on Green Energy and Technology (ICGET) 2015 Sep 11 (pp. 1-5). IEEE.
12. Pastuszak J, Węgierek P. Photovoltaic cell generations and current research directions for their development. Materials. 2022 Aug 12;15(16):5542.

13. Rhaman MM, Matin MA. Organic Solar Cells: Historical developments and challenges. In2015 International Conference on Advances in Electrical Engineering (ICAEE) 2015 Dec 17 (pp. 26-29). IEEE.
14. Mazumdar SC, Datta S, Alam F. Structural, magnetic and transport properties of Gd and Cu co-doped $BiFeO_3$ multiferroics. *J Appl Math Phys.* 2022;10(6):2026–203.
15. Rhaman MM, Matin MA, Hakim MA, Islam MF. Dielectric, ferroelectric and ferromagnetic properties of samarium doped multiferroic bismuth ferrite. Materials Research Express. 2019 Dec 1;6(12):125080.
16. Hill NA. Why are there so few magnetic ferroelectrics?. The journal of physical chemistry B. 2000 Jul 27;104(29):6694-709.
17. Rhaman MM, Matin MA, Hossain MN, Khan MN, Hakim MA, Islam MF. Ferromagnetic, electric, and ferroelectric properties of samarium and cobalt co-doped bismuth ferrite nanoparticles. Journal of Physics and Chemistry of Solids. 2020 Dec 1;147:109607.
18. Rao CN, Serrao CR. New routes to multiferroics. Journal of Materials Chemistry. 2007;17(47):4931-8.
19. Rhaman MM, Matin MA, Al Mamun MA, Hussain A, Hossain MN, Das BC, Hakim MA, Islam MF. Enhanced electrical conductivity and multiferroic property of cobalt-doped bismuth ferrite nanoparticles. Journal of Materials Science: Materials in Electronics. 2020 Jun;31(11):8727-36.
20. Prasad SR, Sreenivasulu G, Roopas Kiran S, Balasubramanian M, Murty BS. Electrical and magnetic properties of nanocrystalline $BiFeO_3$ prepared by high energy ball milling and microwave sintering. Journal of Nanoscience and Nanotechnology. 2011 May 1;11(5):4097-102.
21. Rhaman MM, Matin MA, Hossain MN, Mozahid FA, Hakim MA, Rizvi MH, Islam MF. Bandgap Tuning of Sm and Co Co-doped BFO Nanoparticles for Photovoltaic Application: Rhaman, Matin, Hossain, Mozahid, Hakim, Rizvi, and Islam. Journal of Electronic Materials. 2018 Dec;47(12):6954-8.
22. Selbach SM, Tybell T, Einarsrud MA, Grande T. Size-dependent properties of multiferroic $BiFeO_3$ nanoparticles. Chemistry of materials. 2007 Dec 25;19(26):6478-84.
23. Rhaman MM, Matin MA, Hossain MN, Mozahid FA, Hakim MA, Islam MF. Bandgap engineering of cobalt-doped bismuth ferrite nanoparticles for photovoltaic applications. Bulletin of Materials Science. 2019 Aug;42(4):190.
24. Sakar M, Balakumar S, Saravanan P, Jaisankar SN. Annealing temperature mediated physical properties of bismuth ferrite ($BiFeO_3$) nanostructures synthesized by a novel wet chemical method. Materials Research Bulletin. 2013 Aug 1;48(8):2878-85.
25. Rhaman MM, Matin MA, Hakim MA, Islam MF. Bandgap tuning of samarium and cobalt co-doped bismuth ferrite nanoparticles. Materials Science and Engineering: B. 2021 Jan 1;263:114842.
26. Valant M, Axelsson AK, Alford N. Peculiarities of a solid-state synthesis of multiferroic polycrystalline $BiFeO_3$. Chemistry of Materials. 2007 Oct 30;19(22):5431-6.
27. Matin MA, Rhaman MM, Hakim MA, Islam MF. $Bi_{(1-y)}Sm_yFeO_3$ as prospective photovoltaic materials: MA MATIN et al. Bulletin of Materials Science. 2020 Dec;43(1):167.
28. Kim JK, Kim SS, Kim WJ. Sol–gel synthesis and properties of multiferroic $BiFeO_3$. Materials Letters. 2005 Dec 1;59(29-30):4006-9.
29. Niloy NR, Chowdhury MI, Anowar S, Islam J, Rhaman MM. Structural and optical characterization of multiferroic $BiFeO_3$ nanoparticles synthesized at different annealing temperatures. *J Nano-Electron Phys.* 2020;12(5):05015. doi:10.21272/jnep.12(5).05015
30. Rhaman MM, Matin MA, Hakim MA, Islam MF. Optical and electrical properties of impurity-less multiferroic bismuth ferrite nanoparticles. Materials Science and Engineering: B. 2022 Jan 1;275:115501.
31. Hossain MN, Matin MA, Islam MM, Rhaman MM, Hakim MA, Islam MF. Aspects of Structural and Multiferroic Properties of A-(15% Gd) and B-Site (5–15% Cr) Doped Perovskite $BiFeO_3$ Nanoparticles. Transactions on Electrical and Electronic Materials. 2021 Aug;22(4):543-9.

32. Hossain MN, Matin MA, Rhaman MM, Ali MA, Hakim MA, Roy SK. Structural and Dielectric Progression of 5% Gd Doped $BiFeO_3$ Nanoparticles Through Cr (2-8%) Doping. Journal of Engineering Science. 2021;12(3):101-10.
33. Mohsin TB, Islam SA, Tonni TT, Rhaman MM. Analysis of conductivity and band-gap energy of bismuth ferrite nanoparticles as prospective photovoltaic material. Materials Today: Proceedings. 2023 Feb 8.
34. Hedge MS, Aruna ST, Rattan T, Patil KC. Chemistry of nanocrystalline oxide materials: combustion synthesis, properties and applications. World scientific; 2008 Sep 8.
35. Rhaman MM, Miah MS, Ahmad T. Investigation of magnetic and electric properties of bismuth ferrite nanoparticles at different temperatures. Nano-Structures & Nano-Objects. 2024 Sep 1;39:101304.
36. Matin MA, Rhaman MM, Hossain MN, Mozahid FA, Hakim MA, Rizvi MH, Islam MF. Effect of preparation routes on the crystal purity and properties of $BiFeO_3$ nanoparticles. Transactions on Electrical and Electronic Materials. 2019 Dec;20(6):485-93.
37. Jaiswal A, Das R, Vivekanand K, Mary Abraham P, Adyanthaya S, Poddar P. Effect of reduced particle size on the magnetic properties of chemically synthesized $BiFeO_3$ nanocrystals. The Journal of Physical Chemistry C. 2010 Feb 11;114(5):2108-15.
38. Rojas-George G, Silva J, Castañeda R, Lardizábal D, Graeve OA, Fuentes L, Reyes-Rojas A. Modifications in the rhombohedral degree of distortion and magnetic properties of Ba-doped $BiFeO_3$ as a function of synthesis methodology. Materials Chemistry and Physics. 2014 Jul 15;146(1-2):73-81.
39. Rhaman MM, Rahman N, Akther S, Islam MA, Hasan SK. Optical and Structural Property Analysis of Samarium and Cobalt Co-doped Bismuth Ferrite Nanoparticles. In2024 6th International Conference on Sustainable Technologies for Industry 5.0 (STI) 2024 Dec 14 (pp. 1-5). IEEE.
40. Efaz ET, Rhaman MM, Imam SA, Bashar KL, Kabir F, Mourtaza ME, Sakib SN, Mozahid AF. A review of primary technologies of thin-film solar cells. Engineering Research Express. 2021 Sep 1;3(3):032001.
41. Ihlefeld JF, Podraza NJ, Liu ZK, Rai RC, Xu X, Heeg T, Chen YB, Li J, Collins RW, Musfeldt JL, Pan XQ. Optical band gap of $BiFeO_3$ grown by molecular-beam epitaxy. Applied Physics Letters. 2008 Apr 7;92(14).
42. Jindata W, Musikajaroen S, Wongpratat U, Jaisuk C, Wongprasod S, Tanapongpisit N, Laohana P, Sripallawit N, Thiwatwaranikul T, Muenwacha T, Khajonrit J. Enhanced energy density of $LiNi_{0.5}Mn_{0.3}Co_{0.2}O_2$ batteries with negative-electronic-compressibility thin film coating. Applied Physics Letters. 2024 Jul 22;125(4).
43. Machado P, Cano I, Menéndez C, Cazorla C, Tan H, Fina I, Campoy-Quiles M, Escudero C, Tallarida M, Coll M. Enhancement of phase stability and optoelectronic performance of $BiFeO_3$ thin films via cation co-substitution. Journal of Materials Chemistry C. 2021;9(1):330-9.
44. Islam MZ, Hasan M, Rahman MF, Rhaman MM. DFT-based insights into Ca, Mg, and Cr-doped $BaNpO_3$ perovskites for advanced optoelectronic applications. Next Materials. 2025 Jul 1;8:100538.
45. Zemene S, Yohannes YB, Wubetu GA. Synthesis and characterization of undoped and Co-doped Bismuth Ferrite nanoparticles for photovoltaic applications. Physica Scripta. 2025 Jan 1;100(1):0159a5.
46. Rhaman MM, Matin MA, Hossain NM, Hakim MA, Islam MF. Prospect and barrier of multiferroic bismuth ferrite for application in solar cell. In2019 2nd international Conference on innovation in Engineering and Technology (ICIET) 2019 Dec 23 (pp. 1-5). IEEE.
47. Kebede MT, Dillu V, Devi S, Chauhan S. Phase transition and optical properties of samarium-doped $BiFeO_3$ nanoparticles. Journal of Materials Science: Materials in Electronics. 2020 Nov;31(22):19950-60.
48. Matin, M. A., Hossain, M. N., Rhaman, M. M., Mozahid, F. A., Ali, M. A., Hakim, M. A., & Islam, M. F. (2019). Dielectric and optical properties of Ni-doped $LaFeO_3$ nanoparticles. SN Applied Sciences, 1(11), 1479.

49. Hossain MN, Rhaman MM, Ali MA, Jahan N, Momin AA, Rahman MM, Hakim MA. Novel gadolinium (Gd) and chromium (Cr) co-doped yttrium iron garnet ($Y_3Fe_5O_{12}$) nanoparticles. Arabian Journal for Science and Engineering. 2024 Jul;49(7):9967-82.
50. Catalan G, Scott JF. Physics and applications of bismuth ferrite. Advanced materials. 2009 Jun 26;21(24):2463-85.
51. Yang H, Xian T, Wei ZQ, Dai JF, Jiang JL, Feng WJ. Size-controlled synthesis of $BiFeO_3$ nanoparticles by a soft-chemistry route. Journal of sol-gel science and technology. 2011 Apr;58(1):238-43.
52. Lomanova NA, Osipov AV, Ugolkov VL, Kenges KM, Yastrebov SG. Facile solution combustion synthesis of $BiFeO_3$ nanopowder with improved magnetic and photocatalytic characteristics. Inorganic Chemistry Communications. 2025 Aug 1;178:114591.
53. 1.Niloy NR, Chowdhury MI, Shanto MAH, Islam J, Rhaman MM. Multiferroic Bismuth ferrite nanocomposites as a potential photovoltaic material. IOP Conf Ser: Mater Sci Eng [Internet]. 2021 Feb 1;1091(1):012049. Available from: http://dx.doi.org/10.1088/1757-899x/1091/1/012049.
54. Awni AG, Abbas ZM. Morphological and structural properties of bismuth-nickel ferrite synthesized by a combined sol-gel method. Nexo Revista Científica. 2023 Dec 31;36(06):1076-86.
55. Gil-González E, Perejón A, Sánchez-Jiménez PE, Sayagués MJ, Raj R, Pérez-Maqueda LA. Phase-pure BiFeO 3 produced by reaction flash-sintering of Bi_2O_3 and Fe_2O_3. Journal of Materials Chemistry A. 2018;6(13):5356-66.
56. Yuan H, Pal S, Forrester C, He Q, Briscoe J. Understanding the impact of Bi stoichiometry towards optimised $BiFeO_3$ photocathodes: structure, morphology, defects and ferroelectricity. Journal of Materials Chemistry A. 2024;12(28):17422-31.
57. Sahoo P, Dixit A. Interband electronic transitions and optical phonon modes in size-dependent multiferroic $BiFeO_3$ nanoparticles. Physical Chemistry Chemical Physics. 2024;26(12):9675-86.
58. Tauc J, editor. Amorphous and liquid semiconductors. Springer Science & Business Media; 2012 Dec 6.
59. Rhaman MM. Comparative Sol–Gel Synthesis Approaches for $BiFeO_3$ Nanoparticles for Photovoltaic Solar Cell Applications. Journal of Advancements in Material Engineering. 2026 Jan;11(1):1-5.
60. A.K.M. Aktaruzzaman Shuvo, Md Minhazur Rashid Adnan, Md. Samiul Islam, Md. Meganur Rhaman,Influence of annealing temperature on the structural, dielectric, and impedance properties of Sm and Co co-doped $BiFeO_3$ for advanced electronic and energy applications,Next Materials,Volume 11,2026,101967,ISSN 2949-8228.
61. Noguchi Y, Matsuo H. Origin of Ferroelectricity in $BiFeO_3$-Based Solid Solutions. Nanomaterials. 2022 Nov 24;12(23):4163.

